Available online at www.sciencedirect.com
ScienceDirect
International Journal of Heat and Mass Transfer 50 (2007) 2414–2424
International Journal of HEAT and MASS TRANSFER
www.elsevier.com/locate/ijhmt

Heat transfer improvement by arranging detached ribs on suction surfaces of rotating internal coolant passages

Tong-Miin Liou *, Yi-Sian Hwang, Meng-Yu Chen

Department of Power Mechanical Engineering, National Tsing Hua University, Hsinchu 30013, Taiwan, ROC

Received 30 January 2006
Available online 27 February 2007

Abstract

Heat transfer coefficient, flow field, and wall static pressure distributions were measured in a rotating two-pass square duct with detachment of 90° ribs from the first pass leading wall and second pass trailing wall as well as attachment of 90° ribs onto the other two opposite walls. Laser-Doppler velocimetry was used to measure the local flow velocity. The ribs were square in cross-section and their detached-distance/height ratio was 0.38. The rib-height/duct-height ratio and the pitch/rib-height ratio were 0.136 and 10, respectively. Duct Reynolds number was fixed at 1×10^4 and rotating number ranged from 0 to 0.2. Results are documented in terms of the main flow development, cross-stream secondary flow structure, the distributions of the pressure coefficient, the variation of friction factor with *Ro*, and passage averaged Nusselt number ratios under constant flow rate and constant pumping power conditions. For CFD reference, the periodic fully developed rotating flow condition is attained after the 6th rib pair in the first pass. In addition, the relationships between the regional averaged Nusselt number, transverse and streamwise mean velocity components, and turbulent kinetic energy are addressed. Using these relationships the general superiority of heat transfer enhancement of the attached–detached 90° ribs arrangement over the attached–attached one can be reasonably illustrated. Simple expressions are obtained to correlate the friction factor with *Ro*, which are lacking in the published literature. The respective contributions of the ribs and passage rotation on the passage friction loss are identified.

1. Introduction

Rotation has been reported to more favorably augment surface heat transfer on the first pass trailing wall and second pass leading wall of a serpentine internal cooling duct [1]. However, it is known that poor heat transfer occurs in the wall corner region immediately behind the 90° solid ribs for both stationary and rotating internal coolant ducts [1]. To eliminate the downstream corner vortex of the 90° solid ribs, rib detachment (C in Fig. 1) has been proved to be effective for stationary ducts [2,3]. Thus, to further augment internal cooling for metal blade of a gas turbine engine the present study proposes an alternative arrangement of rib arrays, i.e. detached–attached 90° ribs, with detachment of 90° ribs from the first pass leading wall and second pass trailing wall as well as attachment of 90° ribs onto the other two opposite walls. On the other hand, surface heat transfer is generally augmented with the penalty of increased pressure loss. Thus, efforts should be given for a better understanding of the associated local fluid flow and friction loss such that a better compromise between the heat transfer enhancement and pressure loss can be attained.

Some previous measurements of main and secondary flow structures in single pass rectangular ducts with 90° angled ribs and in two-pass square ducts with 45° rib turbulators were respectively performed by Liou et al. [4] using laser-Doppler velocimetry (LDV) and Schabacker et al. [5], Chanteloup et al. [6], and Elfert et al. [7] using particle image velocimetry (PIV), but the ducts were all stationary. In the following, only flowfield measurements in ribbed rotating ducts relevant to the present study are

---

* Corresponding author. Tel.: +886 3 5742607; fax: +886 3 5729716.
E-mail address: tmliou@pme.nthu.edu.tw (T.-M. Liou).

0017-9310/$ - see front matter © 2007 Elsevier Ltd. All rights reserved.
doi:10.1016/j.ijheatmasstransfer.2006.09.040

Nomenclature

A	half width of duct (m)
B	half height of duct (m)
C	stand off distance between rib and wall (m)
C_p	pressure coefficient, $(P - P_0)/(0.5\rho U_b^2)$
D_H	hydraulic diameter, $4AB/(A+B)$ (m)
f	friction factor (constant flow rate), $(\Delta P/\Delta X) \cdot D_H/(\rho U_b^2/2)$ along a selected wall (ΔX includes two straight passes and a turn in the calculation)
f^*	friction factor (constant pumping power), $(\Delta P/\Delta X) \cdot D_H/(\rho U_b^2/2)$
h	heat transfer coefficient ($\mathrm{W\,m^{-2}\,K^{-1}}$)
H	rib height (m)
K	two-dimensional turbulent kinetic energy $(\overline{u^2}+\overline{v^2})/2$ ($\mathrm{m^2\,s^{-2}}$)
k_a	thermal conductivity of air ($\mathrm{W\,m^{-1}\,K^{-1}}$)
Nu	local Nusselt number, $h \cdot D_H/k_a$
Nu_0	Nusselt number in fully developed tube flow, $0.023 \cdot Re^{0.8} \cdot Pr^{0.4}$
Nu_p	pass averaged Nusselt number
Nu_p^*	pass averaged Nusselt number (constant pumping power)
Nu_0^*	Nusselt number in fully developed tube flow, $Nu_0^* = 0.023\ Re^{*0.8} Pr^{0.4}$ (constant pumping power)
Nu_{rg}	regional averaged Nu
N	rib index
P	wall static gage pressure ($\mathrm{N\,m^{-2}}$)
P_0	pressure at inlet reference station $X^* = 11.6$ in first pass ($\mathrm{N\,m^{-2}}$)
Pi	rib pitch (m)
Pr	Prandtl number of air, ν/α
R	radii of rib's rounds and fillets (m)
Re	Reynolds number (constant flow rate), $U_b D_H/\nu$
Re^*	Reynolds number (constant pumping power), $U_b D_H/\nu$
Ro	rotation number, $\omega D_H/U_b$
U	streamwise mean velocity ($\mathrm{m\,s^{-1}}$)
U_b	duct bulk mean velocity ($\mathrm{m\,s^{-1}}$)
u	streamwise velocity fluctuation ($\mathrm{m\,s^{-1}}$)
u'	rms value of streamwise velocity fluctuation, $\sqrt{\overline{u^2}}$ ($\mathrm{m\,s^{-1}}$)
V	transverse mean velocity ($\mathrm{m\,s^{-1}}$)
v	transverse velocity fluctuation ($\mathrm{m\,s^{-1}}$)
v'	rms value of transverse velocity fluctuation, $\sqrt{\overline{v^2}}$ ($\mathrm{m\,s^{-1}}$)
W	rib width (m)
W_d	divider thickness (m)
X	streamwise coordinate, Fig. 1 (m)
X^*	normalized streamwise coordinate, X/D_H
X_N	streamwise coordinate in a pitch, Fig. 4 (m)
Y	transverse coordinate, Fig. 1 (m)
Y^*	normalized transverse coordinate, Y/B
Y_N	transverse coordinate in a pitch, Fig. 4 (m)
Z	spanwise coordinate, Fig. 1 (m)
Z^*, Z^{**}	normalized spanwise coordinate, (i) $X < 0$, $Z^{**} = Z/(2A + W_d/2)$ (in the turn) (ii) $X \geqslant 0$, $Z < 0$, $Z^* = (Z + W_d/2)/2A$ (in the first pass) (iii) $X \geqslant 0$, $Z > 0$, $Z^* = (Z - W_d/2)/2A$ (in the second pass)

Greek symbols

α	thermal diffusivity of air ($\mathrm{m^2/s}$)
θ	coolant passage orientation, Fig. 1 (°)
ν	kinematic viscosity of air ($\mathrm{m^2/s}$)
ρ	air density ($\mathrm{kg/m^3}$)
ω	rotating speed ($\mathrm{rad\,s^{-1}}$)
Ω	vorticity ($\mathrm{s^{-1}}$)

Subscripts

b	bulk
max	maximum value
s	smooth
x	streamwise component

cited. For coolant passage orientation $\theta = 0°$ (Fig. 1), Iacovides et al. [8–10] reported laser-Doppler velocimetry and wall pressure measurements in a two-pass passage for assessment of turbulence models used in the computation of blade-cooling flows. In both passes, the leading and trailing walls were roughened with 90° angled ribs of square cross-section in a staggered arrangement. It should be mentioned that the cross-stream secondary flow development for $Ro \neq 0$ were not investigated by these researchers.

For passage orientation $\theta = 90°$, Tse and Steuber [11] studied mean flow characteristics in a rotating four-pass coolant passage using LDV. Their ribs having a semi-circular cross-section were skewed −45° and +45°, respectively to the radially outward and inward main stream and arranged in a staggered mode. Reynolds number (Re) and rotating number were fixed at 25,000 and 0.24, respectively. Secondary flow structures around the turn were presented in detail; however, turbulence quantities were not reported. Liou et al. [1] studied fluid flow in a rotating two-pass duct with in-line 90° ribs. The ribs were square in cross-section. Their LDV data were presented with Re fixed at 1×10^4 and Ro varied from 0 to 0.2. The rotating ribbed duct flow was found to produce higher U_{max}/U_b and u'_{max}/U_b, stronger total averaged secondary flow, and higher heat transfer enhancement. Keeping the same operating conditions, they further performed LDV and pressure measurements for in-line [12] and staggered [13] 45° ribs. Among these studies, the absence of a fully developed flow condition in the rotating 45° ribbed passage was concluded in [12,13]. Servouze and Sturgis [14] presented flow field

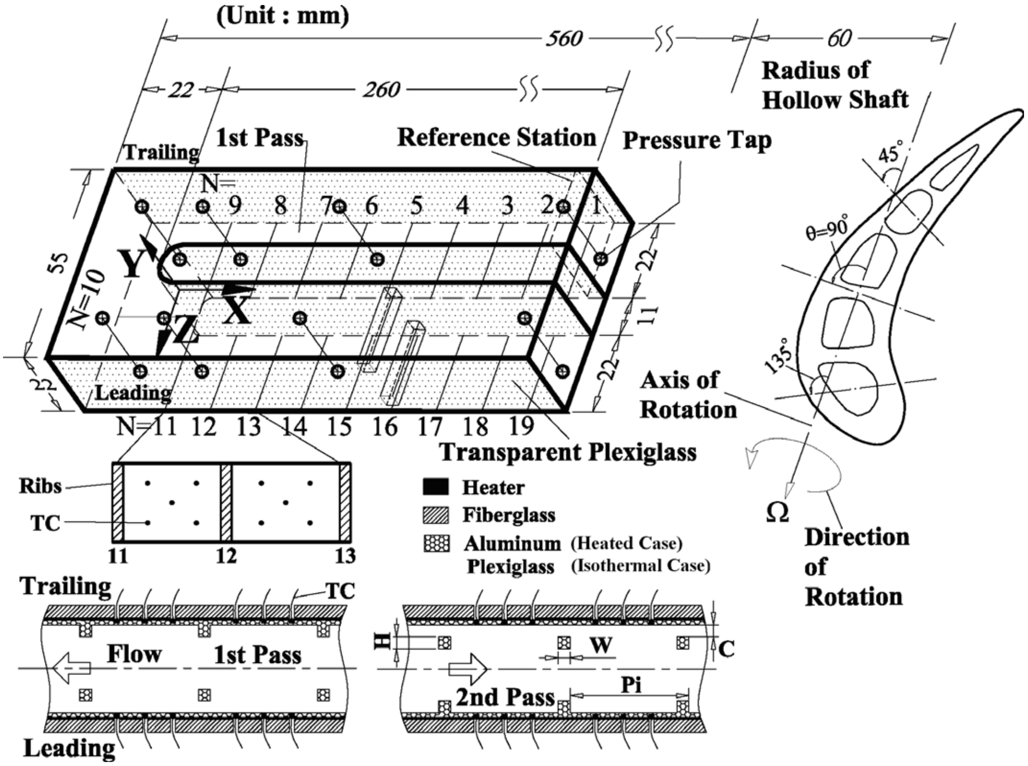

Fig. 1. Sketch of configuration, coordinate system, and dimension of test section.

measurements in one branch of a two-pass coolant passage with in-line 60° square ribs under adiabatic conditions using 2-D PIV. They presented average velocity fields at $Ro = 0$, 0.06 for $Re = 25{,}000$ and $Ro = 0$, 0.33 for $Re = 5000$. There were no measurements of the cross-stream secondary flow development. No separation bubble on the inner partition wall immediately downstream of the bend was observed, similar to that concluded by Liou et al. in [1].

Computationally, Prakash and Zerkle [15] showed that Coriolis effects ($Ro = 0.12$) are less pronounced in a 90° ribbed passage compared to a smooth wall passage. Iacovides and Raisee [16] found that the isotropic eddy viscosity model and the widely used wall function approach are unable to capture physically reasonable heat transfer and flow field features in serpentine cooling ducts with 90° ribs. This is because the turn and ribs usually generate flow separation and anisotropic turbulence. Jang et al. [17] computed flow and heat transfer in a one-pass rotating square duct with staggered 45° ribs using a Reynolds stress turbulence model. Their results revealed that the Coriolis force, centrifugal buoyancy, and 45° ribs generate strong anisotropic turbulent stresses and heat fluxes. The computations of Lin et al. [18] were based on compressible Navier–Stokes equation and the governing equations were closed by the low Reynolds number SST turbulence model. They examined how Coriolis force, centrifugal buoyancy, and pressure gradients induced by streamline curvature from bends and inclined ribs affect the local flow structure. Obviously, the computational studies cited above all suggest the necessity of detailed fluid flow measurements in a rotating multi-pass ribbed duct with 180° sharp turning. Tafti [19] performed large eddy simulations (LES) of flow and heat transfer in a single-pass rotating passage roughened with in-line 90° ribs. Murata and Mochizuki [20] investigated the effects of Coriolis and buoyancy forces on the turbulent heat transfer disturbed by in-line 90° and 60° ribs in a single pass rotating duct ($Ro = 1.0$) with a square cross-section. In their one-pitch simulations [19,20] fully developed flow and heat transfer conditions in a single-pass channel were assumed. Murata and Mochizuki [21] further extended their periodic boundary conditions to the full two-pass channel case. Tafti [22] also extended his computations to show that for developing flow in a rotating duct with in-line 90° ribs at least nine rib pitches were required to achieve fully developed flow state.

Because measuring fluid flow in rotating ribbed coolant ducts is relatively difficult, the corresponding heat transfer measurements [1,23–28] are more abundant. Fann et al. [27] made local heat transfer measurements in rotating four-pass passage with ribbed surfaces. They concluded that both rotation and ribs improved the local heat transfer, and 45° ribs performed the best in both the stationary and rotating cases. Azad et al. [28] performed experimental heat transfer studies in a two-pass rectangular passage. Their results showed that 45° parallel ribs produced a better heat transfer augmentation than 45° cross ribs.

Although aforementioned studies have provided valuable information, most of previous velocity results reported from measuring these difficult-to-measure flows with passage orientation $\theta = 90°$ did not provide turbulence data and local wall pressure relevant to the friction loss. Turbulence and pressure distribution data will thus be presented in the present work. In addition, ribs will be arranged such that the merits of both rib detachment and rib attachment are preserved, i.e. detachment of 90° ribs from the first pass leading wall and second pass trailing wall as well as attachment of 90° ribs onto the other two opposing walls. Measurements of flow field, heat transfer coefficient, and wall static pressure distribution will be made under various rotation numbers. The main purpose is to relate the fluid flow results to those of heat transfer so as to provide physical explanation to the heat transfer augmentation. In addition, the present heat transfer results are compared with those of previous attached and detached cases. It is believed that the information gathered would provide a more useful reference to the turbine cooling designers.

2. Experimental apparatus and conditions

Fig. 2 provides an isometric depiction of the experimental apparatus consisting of rotor rig, coolant flow system, test section, and LDV system. The two-color LDV system has been described in detail in authors' previous studies [1,4,29]. It measured two velocity components (U, V) in the present study. For the flow system, the inlet air firstly flowed radially outward in the first pass, made a 180° sharp turn, and flowed radially inward in the second pass. A 2.2 kW turbo-blower controlled by a frequency converter was used to drive the air from the test section to ambient. A micro-differential pressure transducer (Kyowa PDL-40GB) connected to 16 pressure taps on the leading and trailing walls (Fig. 1) measured the wall gage pressures. The pressure transducer was located on the wall of the hollow shaft (Fig. 2), i.e. at a radius of 60 mm (Fig. 1). The centrifugal force effect on the deformation of the pressure transducer membrane is thus very small and can be subtracted from the local wall pressure measured. These signals were subsequently amplified and fed via the slip ring to the PC for storage. Note that the micro-differential pressure transducer was referenced to a pressure tap located at the inlet reference station, $X = 255$ mm in Fig. 1. It used a foil strain gage as its detector element and permits high precision measurement of very small differential pressure. Its accuracy is within ±0.1% of the 400 mm Aq (3922 N m^{-2}) full-scale value.

Fig. 1 shows an isometric depiction of the configuration, coordinate system, and dimensions of the test section whose side walls were made of acrylic sheets 20 mm thick for optical access. The top and bottom walls and the ribs of the test section were made of Plexiglas for velocity measurements and aluminum for heat transfer measurements. The flow passages had square cross-section with a hydraulic diameter $D_{\mathrm{H}} = 22$ mm and the divider-wall thickness was $0.5D_{\mathrm{H}}$. At the turn, the clearance between the tip of the divider wall and the duct outer wall was fixed at 1 D_{H}. The cross-section of the ribs was square with $H/D_{\mathrm{H}} = 0.136$ and $Pi/H = 10$ in each pass. The 90° transverse ribs were detached a distance of $C = 0.38$ H from the first pass leading wall and second pass trailing wall as well

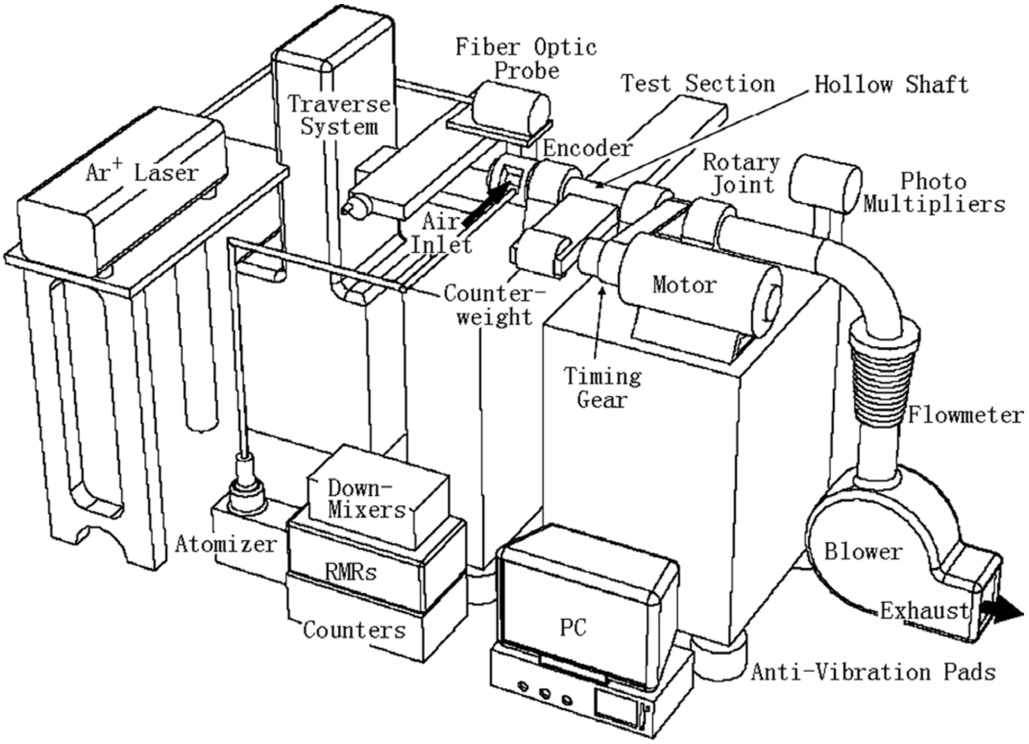

Fig. 2. Schematic drawing of flow system and LDV apparatus.

as attached onto the other two opposite walls. In each pass nine ribs were equally spaced on the leading and trailing walls, respectively. The tips of the first rib pair were located at 13.8 mm downstream of the front edge of the test section. Inside the turn a pair of ribs was also placed at the mid-turn. The Reynolds number, based on the bulk mean air velocity of 7.58 m/s and D_H, was fixed at 1.0×10^4. The rotation number varied from 0 to 0.20, corresponding to rotational speeds from 0 to 660 rpm.

Velocity measurements were performed under isothermal conditions with an acrylic test section. The velocity data were taken at the entrance reference station and in the region 1.5 rib pitches upstream to 1.5 rib pitches downstream of the turn along the longitudinal central plane of each pass, i.e. $Z^* = \pm 0.5$. At each X station the LDV measurements were made at 9–14 locations. Additional measurements at four selected X stations were also made for checking periodic fully developed flow condition. Cross-stream transverse velocity component measurements were performed in the mid-turn cross-section to reveal the secondary flow structure in the turn. In each cross-section plane the LDV measurements were made at 72 locations. The wall pressures were measured at the 16 locations indicated in Fig. 1 along the leading and trailing walls.

The temperature acquisition system was described in detailed in [30] by the authors, including how to calculate the local heat transfer coefficient, how to take into account the heat loss through the test section during rotation, and how to determine the local bulk air temperature by energy balance. Wall temperatures of the test section were measured by 72 copper-constantan thermocouples (T type) distributed along the leading and trailing walls. The Teflon insulated fine gage single thermocouple had a wire diameter of 0.076 mm (0.003 in.). The junction-bead of the thermocouple was 0.2 mm in diameter and was embedded into the center points of the grooves of the aluminum-plate surfaces heated by thermofoils. Inlet and outlet bulk temperatures were also measured by thermocouples. Two 36-channel slip rings were used to transfer the measured temperature signals to a data acquisition card (ADCLONE, ACL-812PG) and a PC for data storage and further processing.

3. Data uncertainty

The uncertainties in the pressure loss measurements are ±0.1%, ±0.5%, and ±0.1% associated with the pressure transducer temperature effect on output, the slip ring noise, and the amplifier noise, respectively. A resultant uncertainty of ±0.52% is thus estimated for the pressure loss data. The corresponding uncertainty in C_p is ±0.64%. For a 95% confidence level, the statistical errors in the mean velocity and turbulence intensity are less than 1.8% and 3.1%, respectively. More detailed uncertainty estimates and velocity bias correlations are included in Liou et al. [1,4,29]. The most proper uncertainty in Nu is estimated to be less than 10% [30].

4. Results and discussion

4.1. U/U_b profiles at inlet reference station

$X^* = 11.6$ (or $X/H = 85$) located at 5H distance upstream of the first rib pair on the trailing wall ($N = 1$ in Fig. 1) of the first outward passage was selected as the inlet reference station. Fig. 3a and b depict the rotation effect on the streamwise mean X-component velocity and turbulence intensity profiles at inlet reference station in two orthogonal lines $Y^* = 0$ and $Z^* = -0.5$, respectively. Note that in this study the sign of U/U_b is positive if U/U_b is along the streamwise direction. On $Z^* = -0.5$ line, the U/U_b and u'/U_b profiles (Fig. 3a) are fairly symmetric with respect to $Y^* = 0$ for $Ro = 0$. As Ro is increased from 0 to 0.2, the skewness [1] of U/U_b and u'/U_b increases monotonically due to the increase of the Coriolis force directed toward the trailing wall ($Y^* = 1$) and, in turn, the steeper mean velocity gradient near the trailing wall. The U and u' peaks can be as high as 1.25 U_b and 0.26 U_b, respectively, for $Ro = 0.2$. The uniform parts of u'/U_b profiles extend to (with respect to $Y^* = 0$) 70% of the channel height and have values of 10.0 ± 0.5%. For CFD reference, the boundary layer thickness defined at 95% U_{max} is $\delta_{95}/H = 1.5/1.5$, 3.5/1.0, 4.1/0.8, 4.4/0.8,

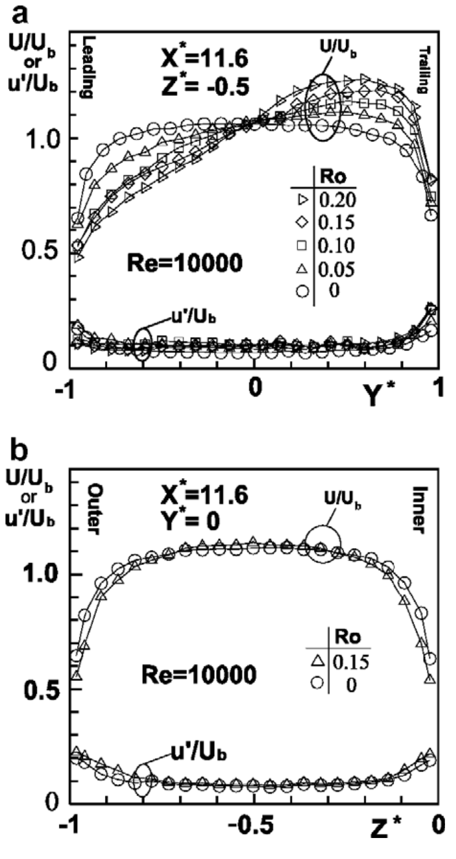

Fig. 3. Rotation effect on longitudinal mean velocity and turbulence intensity profiles at inlet reference station $X^* = 11.6$ of the first pass in two orthogonal lines (a) $Y^* = 0$ (central or mid-span line) and (b) $Z^* = -0.5$ (central or mid-transverse line).

4.6/1.0 along the leading /trailing wall for $Ro = 0$, 0.05, 0.10, 0.15, and 0.2, respectively.

Since the span line $Y^* = 0$ is orthogonal to the Coriolis force, all the U/U_b and u'/U_b profiles on $Y^* = 0$ line (Fig. 3b) are very symmetric to $Z^* = -0.5$. The peak U and u', respectively increase from 1.11 U_b and 0.20 U_b at $Ro = 0$ to 1.13 U_b and 0.22 U_b at $Ro = 0.15$. The boundary layer thickness is $\delta_{95}/H = 1.3/1.3$ and 1.8/1.8 along the inner/outer wall for $Ro = 0$ and 0.15, respectively.

It is worth pointing out that for $Ro = 0$ the difference in the values of $\delta_{95}/H = 1.5/1.5$ for the leading/trailing walls and $\delta_{95}/H = 1.3/1.3$ for the inner/outer walls and why these two values of 1.3 are same even after the 90° turn may result from the effects of the flow expansion, turning and settling, and contraction associated with the complicated upstream geometry. As can be seen from Fig. 2 (not to scale), the inlet air drawn from the ambient atmosphere has to make a 90° turn before it is directed into the symmetric square coolant channel (22 × 22 mm) through the hollow shaft. The diameter of the hollow shaft is 50 mm before the 90° turn and 120 mm at the turn. The expanded portion of the hollow shaft is 120 mm long, 60 mm for flow entrance and 60 mm for flow exit. Thus, the hollow shaft at the turn provides the flow turning as well as acts as a settling chamber.

4.2. Spatial periodicity of U/U_b

It is worth of pointing out that fully developed flow condition is often assumed by researchers in performing LES of fluid flow and/or heat transfer in a rotating ribbed passage for internal cooling of turbine blades [19,20]. Thus, Fig. 4 is presented to examine this assumption via a comparison of the longitudinal mean velocity profiles at a fixed station $X_N/H = 4.5$ but in different pitches $(X_{N+1} - X_N)/H$, $N = 4$–7 in the first pass and $N = 13$–16 in the second pass. The data shown are away from the entrance of the first pass, the 180° turn, and the exit of the second pass. It is found from Fig. 4a that the maximum difference is 25% of U_b between X_5/H and X_6/H profiles (U/U_b) and 4% of U_b between X_6/H and X_7/H profiles, respectively. Hence, the rotating duct flow does not attain a fully developed state up to the 6th rib pair of the first pass. Nevertheless, the maximum differences between any two consecutive profiles in Fig. 4b are from 16% of U_b to 38% of U_b in the second pass. Thus, a fully developed flow condition is never attained in the second pass of the rotating duct investigated due to the complex flow structure generated by the 180° sharp turn and the finite length of the duct. Note that all data presented above are for the rotating case. A similar examination of the stationary case was also performed by the authors. The results show the attainment of a fully developed state after the 4th rib pair. It is interesting to mention that Bonhoff et al. [31] in their PIV measurements in the upstream leg of stationary ribbed duct flows reported that a fully developed flow condition in terms of mean velocity and turbulent kinetic energy was achieved after 3 and 10 rib pitches, respectively, for staggered 90° ribs.

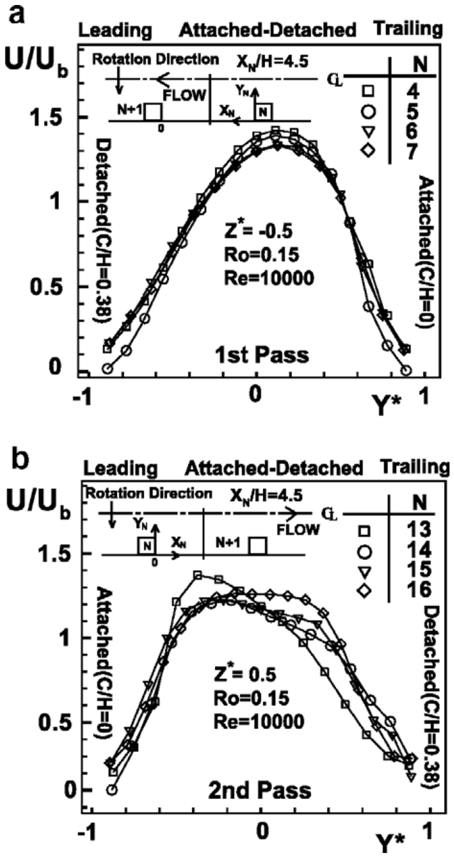

Fig. 4. Examination of periodic fully developed condition by comparing U/U_b profiles at $X_N/H = 4.5$ in various pitches for $Ro = 0.15$ and $Re = 1.0 \times 10^4$.

4.3. Development of main flow

The development of streamwise mean velocity profile along the $Z^* = -0.5$ and $Z^* = +0.5$ plane for the case of $Ro = 0.15$ is depicted in Fig. 5. As fluid flows radially outward (Fig. 5a) over the first attached–detached rib pair, the U/U_b at $X^* = 10.2$ station decreases in the region $|Y^*| \geqslant 0.6$ due to rib's blockage but must increase in the region $|Y^*| < 0.6$ due to mass conservation. The profile is still skewed toward the trailing wall as a result of the Coriolis force; however, the peak of U/U_b moves back towards the centerline, i.e. from $Y^* = 0.6$ to $Y^* = 0.4$, due to the effect of rib's blockage and has a value 1.53 U_b. For the present attached–detached ribbed duct rotating at $Ro = 0.2$, the peak U is 1.58 U_b while it is 1.49 U_b for the case of attached–attached rib pairs at the same Ro [1]. It is obvious that an attached–detached rib arrangement has a larger nozzle or contraction effect (or smaller transverse rib–rib gap). In the second pitch at $X^* = 8.8$, the peak U having a value 1.42 U_b moves further closer to the centerline and occurs at $Y^* = 0.1$. The mean velocity profile looks much more symmetric.

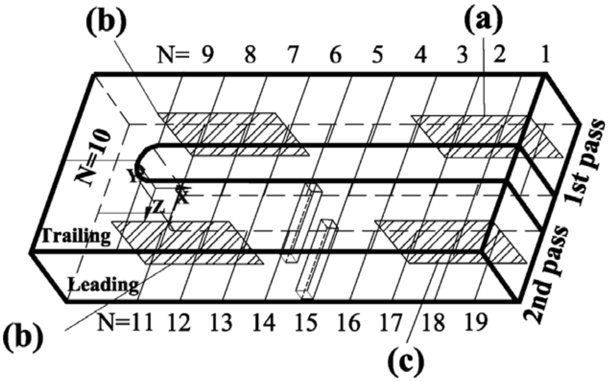

(a) Near the Entry

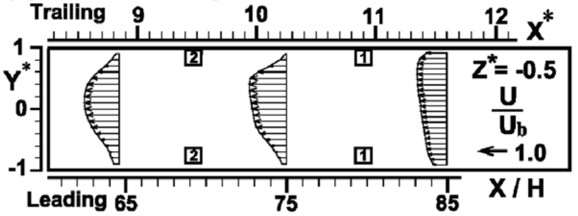

(b) Near the Turn

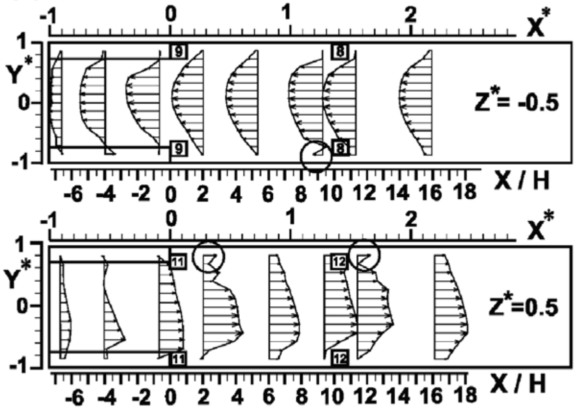

(c) Near the Exit

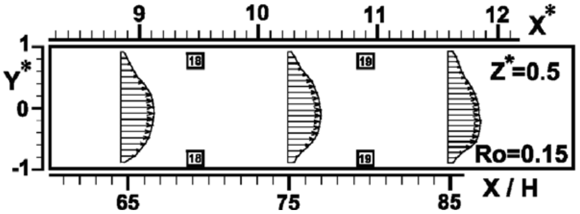

Fig. 5. Evolution of longitudinal mean velocity component in $Z^* = -0.5$ and $Z^* = 0.5$ planes for $Re = 1.0 \times 10^4$ and $Ro = 0.15$: (a) near the entry, (b) around the turn, and (c) near the exit.

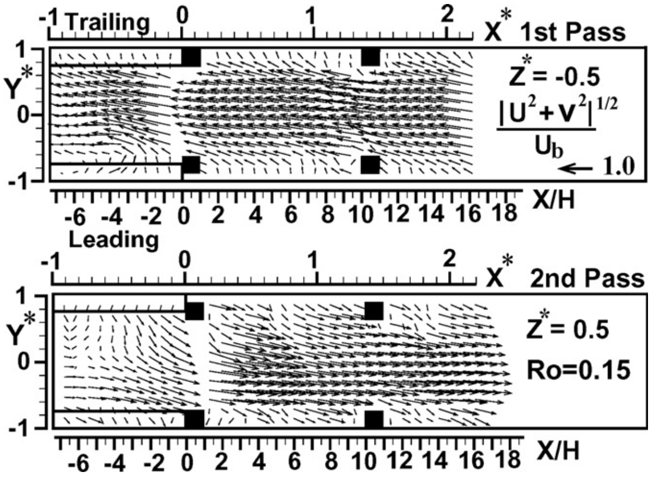

Fig. 6. Mean velocity vector plots around the turn for $Re = 1.0 \times 10^4$ and $Ro = 0.15$ in X–Y plane of the first and second passage.

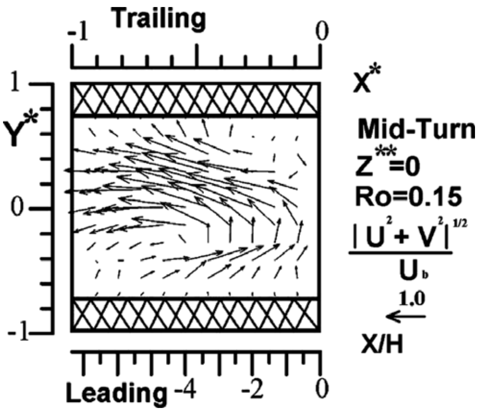

Fig. 7. Mean velocity vector plot on the mid-turn cross-section ($Z^{**} = 0$) for $Re = 1.0 \times 10^4$ and $Ro = 0.15$.

Around the turn, $X^* = 2.2$ to -1 in Fig. 5b, the circled portion of U/U_b profiles immediately downstream of the rib pairs reveals the wake feature of the detached rib. The corresponding mean velocity vector plot in Fig. 6 further unveils the slant impingement of fluid flow upon the first pass trailing wall and second pass leading wall directed by the Coriolis force. Heat transfer on these two corresponding walls is to be enhanced. Within the 180° sharp turn ($-1 < X^* < 0$ or $-7.3 < X/H < 0$), the curvature and rotation make the flow pattern form a strongly skewed Dean-type vortex flow, as clearly shown by Fig. 7, Figs. 6 and 5b. Note that the velocity components normal to the passage tip as well as normal to the leading or trailing wall play an important role in augmenting heat transfer. Inside the turn ($-1 < X^* < 0$) on the first outward duct side, the top portion of Fig. 6 depicts that the near wall mean velocity vectors in the region ($0.8 < Y^* < 1$ and $-1 < X^* < 0$, $Z^* = -0.5$) have larger Y-component and are directed toward the trailing wall ($Y^* = 1$). The downwash (or impinging) effect is expected to markedly increase the heat transfer rate. In contrast, the near-wall mean velocity vectors in the region ($-1 < Y^* < -0.8$ and $-0.7 < X^* < 0$, $Z^* = -0.5$) have larger Y-component but are directed away from the leading wall (upwash effect). Similarly, inside the turn ($-1 < X^* < 0$) on the second pass side ($Z^* = 0.5$), the larger Y-component directed towards the leading wall ($Y^* = -1$, the bottom portion of Fig. 6) suggests heat transfer enhancement inside the turn on the second pass side is higher on the leading wall than on the trailing wall.

Near the exit (Fig. 5c), the skewness of peak velocity toward the leading wall is resulting from the Coriolis force acting on a radially inward duct flow.

4.4. Surface heat transfer and fluid flow

The curve with square symbol in the upper part of Fig. 8 shows the region-averaged (area-weighted) Nusselt number ratio (Nu_{rg}/Nu_0) distributions measured in the present study. The heat transfer coefficient distributions in the first and second passages show different dependences on rotation, primarily due to the reversal of the Coriolis forces acting on the moving fluid in radially outward and inward flows. It is well worth relating the flowfield results to the heat transfer results. The region-averaged X and Y mean velocity components ($U_{\mathrm{rg}}/U_{\mathrm{b}}$, $V_{\mathrm{rg}}/U_{\mathrm{b}}$) and the region-averaged turbulent kinetic energy $K_{\mathrm{rg}}/U_{\mathrm{b}}^2$ measured along the lines, passing through the thermocouple locations (Fig. 1), at 1.5 mm away from the leading and trailing walls are respectively depicted in the middle and lower parts of Fig. 8. The fluid flow results reveal that the distributions of $K_{\mathrm{rg}}/U_{\mathrm{b}}^2$ are approximately similar to those of Nu_{rg}/Nu_0. In other words, turbulence enhances the heat transfer, as expected. The magnitude and direction of the mean transverse velocity component V_{rg} are also essential to the heat transfer enhancement on the leading and trailing walls. The positive values of $-V_{\mathrm{rg}}/U_{\mathrm{b}}$ and $V_{\mathrm{rg}}/U_{\mathrm{b}}$ near the leading and trailing walls, respectively, denote the downwash (or impingement) effect whereas the negative values indicate the upwash effect, as a result of the secondary flow induced by the Coriolis force, geometric turn, and ribs (for flow inside the turn and in the second passage). Note that the downwash destroys the wall boundary layer and brings the cold core fluids onto the heat transfer surface to enhance the heat transfer. The upwash simply carries the fluids (hotter or not so hot depending on the uniformity of heat transfer distribution) away from the heat transfer surface. Fig. 8 depicts that near the first pass trailing wall (region indices: −3, −2, −1) and the second pass leading wall (region indices: 1, 2, 3), the downwash effect of the secondary flow markedly reinforces the heat transfer enhancement on the corresponding walls while the upwash effect only makes noticeable heat transfer augmentation in the regions with the index of −1 and 1. As for the convective effect denoted by $U_{\mathrm{rg}}/U_{\mathrm{b}}$, Fig. 8 shows it less prominently contributes to the heat transfer enhancement on both the leading and trailing wall.

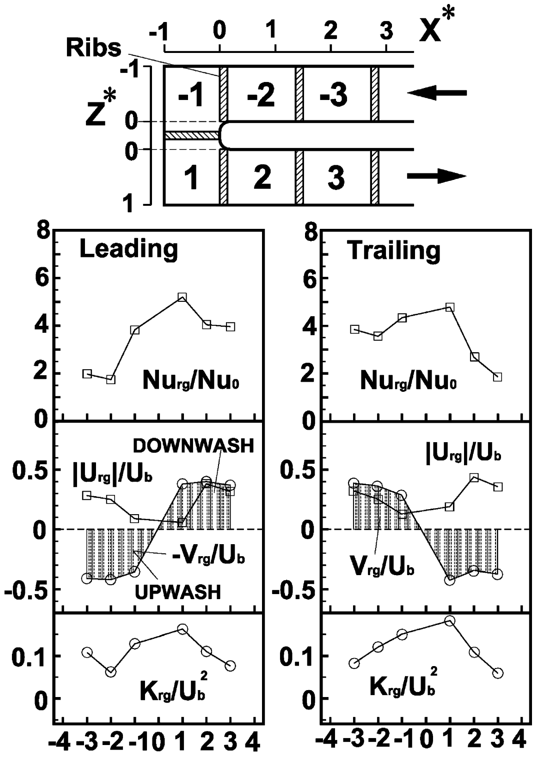

Fig. 8. Relationships between mean velocity components, turbulent kinetic energy, and regional averaged surface heat transfer coefficient (Note that the fluid flow data were taken at 1.5 mm away from the leading and trailing walls).

4.5. Local pressure coefficient and average friction factor

Knowledge of the coolant passage pressure loss will help in designing an efficient rotating cooling system. Nevertheless, the relevant data of local pressure distributions along rotating two-pass coolant ducts is scarce to date. The results are thus plotted in Fig. 9. It is seen that the trend is similar to the familiar pressure distribution along the outer wall of a stationary curved smooth passage. This is

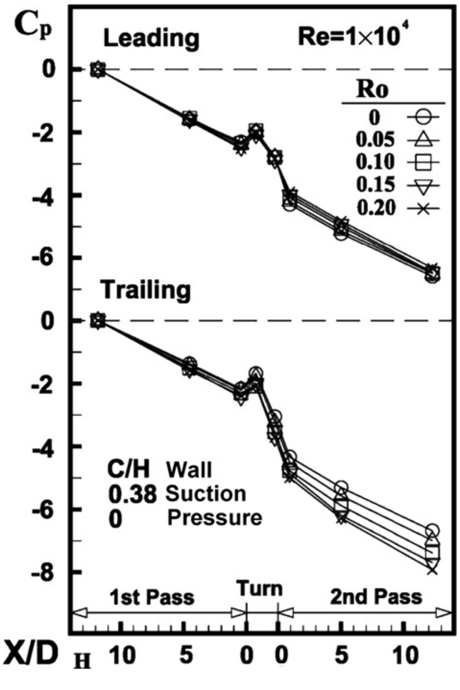

Fig. 9. Variation of dimensionless wall pressure with X/D_{H} at various rotation numbers.

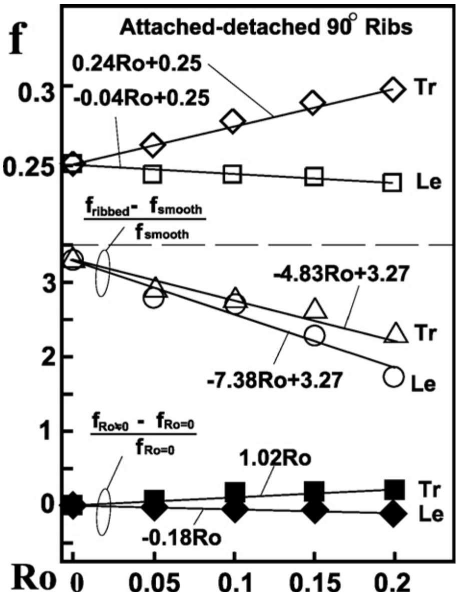

Fig. 10. Friction factor versus rotation number ($Re = 1.0 \times 10^4$, Tr – Trailing, Le – Leading).

because the two pressure taps inside the turn are located on the geometric centerline of the 180° "sharp" turn. These locations are expected to lie to the outer wall side of the flow turning's centerline (Fig. 1). The value of C_p increases and decreases with increasing Ro on the second pass leading wall and trailing wall, respectively.

Fig. 10 depicts the rotation number dependence of average friction factor f in the attached–detached 90°-ribbed passage flow. The maximum deviations of the measured data from the f correlations are 2.1%. The results show an increase of f with increasing Ro on the trailing wall but a slight decrease of f with increasing Ro on the leading wall, respectively. The above trend on the trailing wall is because of the decrease of C_p with increasing Ro on the trailing wall of the second inward duct (Fig. 9). In contrast, the decrease of f with increasing Ro on the leading wall is due to the increase of C_p with increasing Ro on the leading wall of second inward duct toward which the Coriolis force is directed (Fig. 9).

It is interesting to examine the respective effect of ribs and passage rotation on f, as depicted in Fig. 10. It turns out that with ribs and passage rotation the f on the leading/trailing walls increase 180%/230% of f_{smooth} and −4%/20% of $f_{Ro=0}$, respectively, at $Ro = 0.2$. The maximum deviations of the measured data from the $(f_{ribbed}–f_{smooth})/f_{smooth}$ and $(f_{Ro\neq0}–f_{Ro=0})/f_{Ro=0}$ correlations on the leading/trailing walls are 8.2%/5.2% and 2.8%/3.4%, respectively. The correlation equations are listed below:

Along the leading wall

$$f = -0.04\,Ro + 0.25 \tag{1}$$

$$(f_{ribbed} - f_{smooth})/f_{smooth} = -7.38\,Ro + 3.27 \tag{2}$$

$$(f_{Ro\neq0} - f_{Ro=0})/f_{Ro=0} = -0.18\,Ro \tag{3}$$

Table 1
A list of friction factor ratios for two rib configurations examined

$Ro = 0–0.2$ $Re = 1 \times 10^4$	Attached–Attached $f_{at–at}/f_s$	Attached–Detached $f_{at–de}/f_s$
Leading	2.8–3.7	3.3–4.4
Trailing	2.8–3.7	3.1–4.4

at–at: attached–attached; at–de: attached–detached.

Along the trailing wall

$$f = 0.24\,Ro + 0.25 \tag{4}$$

$$(f_{ribbed} - f_{smooth})/f_{smooth} = -4.83\,Ro + 3.27 \tag{5}$$

$$(f_{Ro\neq0} - f_{Ro=0})/f_{Ro=0} = 1.02\,Ro \tag{6}$$

One more comparison worthy of attention is given in Table 1 which lists friction factor ratios for the two interested rib arrangements under the same operating conditions of $Ro = 0$ to 0.2 and $Re = 10{,}000$. It is observed that on the leading/trailing wall the attached–attached and proposed attached–detached ribs generate friction loss approximately 2.8–3.7/2.8–3.7 and 3.3–4.4/3.1–4.4 times that of smooth-walled case. The friction loss is larger for the case of attached–detached ribs largely due to the increase of the wetted surface area (there are four wetted surfaces instead of three), the larger flow contraction and expansion loss as a result of smaller transverse rib–rib space, and the flow contraction and expansion loss through the detached gap (or rib-passage wall gap).

4.6. Comparisons of heat transfer results

Table 2 shows comparisons of passage averaged (averaged over the region indices −3 to +3, Fig. 8) ratios of Nusselt number, mean convective velocity, mean impingement velocity, and turbulent kinetic energy between attached–attached and attached–detached 90° rib arrangements for $Ro = 0.15$. In general, the magnitudes of these flow dynamic data provide the rationale for the superiority of heat transfer enhancement of the attached–detached case over that of the attached–attached one. It is worth pointing out from Table 2 that both the V_{rg}/U_b and K_{rg}/U_b^2 play major roles in the superior heat transfer augmentation attained by the attached–detached 90° ribs.

Table 2 also indicates that the attached–detached case has an average friction factor f of the entire flow passage higher than that of the attached–attached case. The reason has been addressed in the previous section. To take the friction loss into account, Table 3 provides a comparison of the pass averaged Nusselt number ratios under a constant pumping power condition [1–4] for the two rib arrangements examined. The Reynolds number Re^* under a constant pumping power condition was firstly calculated from $f^*Re^{*3} = fRe^3$ where f and f^* were measured under constant flow rate and constant pumping power conditions, respectively. Based on this Re^*, one then performed the measurement of Nu_p^* and the calculation of $Nu_0^* = 0.023\,Re^{*0.8}Pr^{0.4}$. The last column of Table 3 clearly

Table 2
Comparisons of passage averaged quantities (averaged over the indices −3 to +3, Fig. 8) between attached–attached and attached–detached 90° rib arrangements for $Ro = 0.15$ and $Re = 1.0 \times 10^4$

	First pass				Second pass			
	Leading		Trailing		Leading		Trailing	
	at–at	at–de	at–at	at–de	at–at	at–de	at–at	at–de
Nu_{rg}/Nu_0	1.89	2.41	3.93	4.03	4.02	4.25	2.13	2.79
$lU_{rg}l/U_b$	0.35	0.28	0.36	0.27	0.43	0.39	0.42	0.35
$lV_{rg}l/U_b$	0.07	0.37	0.21	0.41	0.15	0.36	0.17	0.39
K_{rg}/U_b^2	0.04	0.09	0.06	0.14	0.07	0.14	0.05	0.15
	Leading				Trailing			
	at–at		at–de		at–at		at–de	
f	0.20		0.24		0.24		0.29	

Table 3
A comparison of regional averaged Nusselt number ratio for two rib configurations examined under a constant pumping power condition

$Ro = 0.20$ $Re = 1 \times 10^4$		Averaged Nusselt number		Compared
		Attached $\left(\frac{Nu_p^*}{Nu_0^*}\right)_{at\text{–}at}$	Detached–Attached $\left(\frac{Nu_p^*}{Nu_0^*}\right)_{at\text{–}de}$	$\frac{(Nu_p^*)_{at\text{–}de}}{(Nu_p^*)_{at\text{–}at}}$
First pass	Leading	1.17	1.54	1.31
	Trailing	2.44	2.52	1.03
Second pass	Leading	2.40	2.58	1.08
	Trailing	1.12	1.55	1.39

indicates the superiority of the proposed attached–detached rib configuration over the attached–attached rib one. More specifically, $(Nu_p^*)_{at\text{–}de}$ can attain $1.03(Nu_p^*)_{at\text{–}at}$ to $1.39(Nu_p^*)_{at\text{–}at}$.

It is also interesting to compare the heat transfer enhancement attained in the present study with that reported by the previous researchers. In Fig. 11 the solid and empty circled curves denote the heat transfer results reported by Azad et al. [28] and Johnson et al. [26] in their thermocouple measurements of surface heat transfer for parallel and staggered attached–attached 45° ribs, respectively, under rotating conditions. It is observed that in general the present attached–detached parallel 90° ribs achieve a relatively higher heat transfer augmentation than that of the smooth-walled cooling passage, approximately 1.7–5.2 Nu_o. It is worth of pointing out that the study on the 45° angle ribbed channel flow reported by Johnson et al. [26] was operated at $Re = 25{,}000$. Their measurements give lower values of Nu_{rg}/Nu_o ranging from 2 to 3.5 partly due to their Re being 2.5 times that of the present case. In general, Nu_{rg}/Nu_o decreases with increasing Re [14] since the rate of increase of Nu_o with increasing Re is over that of Nu_{rg}. Also note that the three results shown in Fig. 11 were taken at somewhat different Ro and H/D_H. The dimensionless rib heights H/D_H of Azad et al. [28] and Johnson et al. [26] are respectively 0.094 and 0.1. These values are lower than 0.136 of the present case. The rib turbulators having lower values of H/D_H are expected to generate lower turbulent kinetic energy K/U_b^2 and, in turn, lower heat transfer enhancement. Similarly, the present case has $Ro = 0.15$ higher than $Ro = 0.11$ and 0.12 of Azad et al. [28] and Johnson et al. [26], respectively, and hence, higher heat transfer augmentation [1]. Further, in the 180° turn both of them do not arrange a rib at the mid turn ($Z^{**} = 0$) whereas there exists a rib at the mid turn to generate additional heat transfer enhancement in the present case.

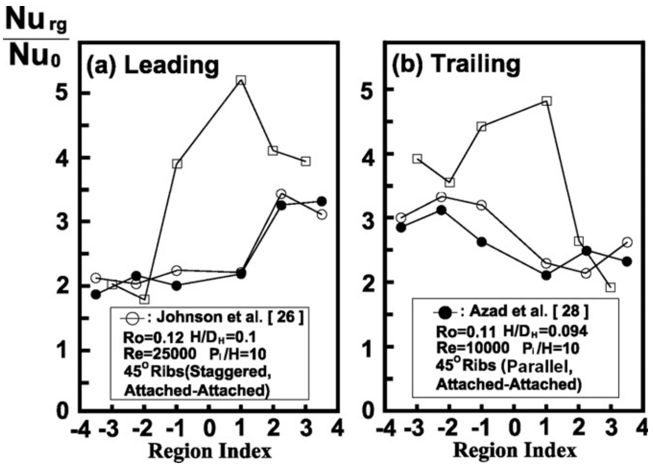

Fig. 11. Comparison of region averaged Nusselt number ratios between various rib arrangements.

5. Concluding remarks

1. The measured streamwise distributions of the region averaged Nussult number ratio on the leading and trailing wall roughened with attached–detached 90° ribs can be reasonably illustrated by the corresponding measured distributions of the region averaged mean convective velocity, mean transverse velocity, and turbulent kinetic energy.
2. The superiority of heat transfer augmentation of the attached–detached 90° ribs over that of attached–attached 90° ribs can be similarly explained by comparing the corresponding values of the aforementioned flow dynamic parameters.
3. Under a constant flow condition, heat transfer augmentation in terms of region averaged Nu achieved by the proposed attached–detached 90° rib pair arrangement

is found to range from 1.7 to 5.2 times that of smooth-walled stationary cooling duct flow.

4. Under a constant pumping power condition with $Ro = 0.2$ and $Re = 10{,}000$, the proposed attached–detached ribs attain heat transfer enhancement about 1.03–1.39 times that of attached–attached ribs.
5. Simple expressions are developed to linearly correlate the friction factor with rotation number for engineering reference. Moreover, the respective effects of the attached–detached 90° ribs and the passage rotation on the cooling passage friction loss have been successfully separated for the first time.
6. For the attached–detached 90° ribbed rotating cooling duct investigated, it is found that the rotating duct flow does not attain a fully developed state up to the 6th rib pair of the first pass. This finding is opposite to the rotating 45° rib case (in-line or staggered) which did not show the fully developed flow condition in the entire first pass. Moreover, a fully developed flow condition is never attained in the second pass of the rotating duct investigated.

Acknowledgement

Support for this work was partially provided by the National Science Council of the Republic of China under contract NSC 93-2212-E-007-019.

References

[1] T.M. Liou, M.Y. Chen, M.H. Tsai, Fluid flow and heat transfer in a rotating two-pass square duct with in-line 90° ribs, ASME J. Turbomach. 124 (2002) 260–268.

[2] T.M. Liou, W.B. Wang, Y.J. Chang, Holographic interferometry study of spatially periodic heat transfer in a channel with ribs detached from one wall, ASME J. Heat Transfer 117 (1995) 32–39.

[3] T.M. Liou, W.B. Wang, Laser holographic interferometry study of developing heat transfer in a duct with a detached rib array, Int. J. Heat Mass Transfer 38 (1) (1995) 91–100.

[4] T.M. Liou, C.C. Chen, Y. Chang, LDV measurements of periodic fully developed main and secondary flows in a channel with rib-disturbed walls, ASME J. Fluids Eng. 115 (1993) 109–114.

[5] J. Schabacker, A. Bolcs, B.V. Johnson, PIV investigation of the flow characteristics in an internal coolant passage with 45° rib arrangement, ASME Paper 99-GT-120 (1999).

[6] D. Chanteloup, Y. Juaneda, A. Bolcs, Combined 3D flow and heat transfer measurements in a 2-pass internal coolant passage of gas turbine airfoil, ASME Paper GT-2002-30214 (2002).

[7] M. Elfert, M.P. Jarius, B. Weigand, Detailed flow investigation using PIV in a typical turbine cooling geometry with ribbed walls, ASME Paper GT-2004-53566 (2004).

[8] H. Iacovides, D.C. Jackson, G. Kelemenis, B.E. Launder, Y.M. Yuan, LDA study of the flow development through an orthogonally rotating U-bend of strong curvature and rib roughened walls, Eng. Turbulence Modeling Exper. 3 (1996) 561–570.

[9] H. Iacovides, D.C. Jackson, H. Ji, G. Kelemenis, B.E. Launder, K. Nikas, LDA study of the flow development through an orthogonally rotating U-bend of strong curvature and rib roughened walls, ASME J. Turbomach. 120 (1998) 386–391.

[10] H. Iacovides, D.C. Jackson, B.E. Launder, Y.M. Yuan, An experimental study of a rib-roughened rotating U-bend flow, Exper. Therm. Fluid Sci. 19 (1999) 151–159.

[11] G.N. Tse, G.D. Steuber, Flow in a rotating square serpentine coolant passage with skewed trips, ASME Paper No. 97-GT-529 (1997).

[12] T.M. Liou, Yi-Sian Hwang, Yi-Chen Li, Pressure and flow characteristics in a rotating two-pass duct with 45° angled ribs, ASME J. Turbomach. 126 (2004) 212–219.

[13] T.M. Liou, Y.S. Hwang, Y.C. Li, Flowfield and pressure measurements in a rotating two-pass duct with staggered rounded ribs skewed 45° to the flow, ASME J. Turbomach. 128 (2006) 340–348.

[14] Y. Servouze, J.C. Sturgis, Heat transfer and flowfield measurements in a rib-roughened branch of a rotating two-pass duct, ASME Paper GT2003-38048 (2003).

[15] C. Prakash, R. Zerkle, Prediction of turbulent flow and heat transfer in a ribbed rectangular duct with and without rotation, ASME J. Turbomach. 177 (1995) 255–264.

[16] H. Iacovides, M. Raisee, Recent progress in the computation of flow and heat transfer in internal cooling passages of turbine blades, Int. J. Heat Fluid Flow 20 (1999) 320–328.

[17] Y.J. Jang, H.C. Chen, J.C. Han, Flow and heat transfer in a rotating square channel with 45° angled ribs by reynolds stress turbulence model, ASME Paper 2000-GT-0229 (2000).

[18] Y.L. Lin, T.I.-P. Shih, M.A. Stephens, M.K. Chyu, A numerical study of flow and heat transfer in a smooth and ribbed U-duct with and without rotation, ASME J. Heat Transfer 123 (2001) 219–232.

[19] D.K. Tafti, Large-Eddy simulations of heat transfer in a ribbed channel for internal cooling of turbine blades, ASME Paper GT-2003-38122 (2003).

[20] A. Murata, S. Mochizuki, Effect of centrifugal buoyancy on turbulent heat transfer in an orthogonally rotating square duct with traverse or angled rib turbulators, Int. J. Heat Mass Transfer 44 (2001) 2739–2750.

[21] A. Murata, S. Mochizuki, Effect of rib orientation and channel rotation on turbulent heat transfer in a two-pass channel with sharp 180° turn investigated by using large Eddy simulations, Int. J. Heat Mass Transfer 47 (2005) 2599–2618.

[22] D.K. Tafti, Large-Eddy simulations of the developing region of a rotating ribbed internal turbine blade cooling channel, ASME Paper GT-2004-53833 (2004).

[23] M.E. Taslim, A. Rahman, S.D. Spring, An experimental investigation of heat transfer coefficients in a spanwise rotating channel with two opposite rib-roughened walls, ASME J. Turbomach. 113 (1991) 75–82.

[24] J.H. Wagner, B.V. Johnson, R.A. Graziani, F.C. Yeh, Heat transfer in rotating serpentine passages with trips normal to the flow, ASME J. Turbomach. 114 (1992) 847–857.

[25] J.A. Parsons, J.C. Han, Y.M. Zhang, Wall heating effect on local heat transfer in a rotating two-pass square channel with 90° rib turbulators, Int. J. Heat Mass Transfer 37 (9) (1994) 1411–1420.

[26] B.V. Johnson, J.H. Wagner, G.D. Steuber, F.C. Yeh, Heat transfer in rotating serpentine passage with trips skewed to the flow, ASME J. Turbomach. 116 (1994) 113–123.

[27] S. Fann, W.J. Yang, N. Zhang, Local heat transfer in a rotating serpentine passage with rib-roughened surfaces, Int. J. Heat Mass Transfer 37 (2) (1994) 217–228.

[28] G.S. Azad, Mohammad J. Uddin, J.C. Han, Heat transfer in a two-pass rectangular channel with 45° angled rib turbulators, ASME Paper 2001-GT-186 (2001).

[29] T.M. Liou, C.C. Chen, M.Y. Chen, Rotating effect on fluid flow in two smooth ducts connected by a 180° bend, ASME J. Fluids Eng. 125 (2003) 327–335.

[30] T.M. Liou, C.C. Chen, Heat transfer in a rotating two-pass smooth passage with a 180° rectangular turn, Int. J. Heat Mass Transfer 42 (1999) 231–247.

[31] B. Bonhoff, J. Schabacker, S. Parneix, J. Leusch, B.V. Johnson, A. Bolcs, Experimental and numerical study of developed flow and heat transfer in coolant channels with 45° and 90° ribs, ASME Paper 99-GT-123 (1999).